Journal of Advanced Ceramics
2023, **12**(4): 711–723
https://doi.org/10.26599/JAC.2023.9220714
ISSN 2226-4108
CN 10-1154/TQ

Research Article

Construction of *hydrangea*-like core–shell SiO_2@$Ti_3C_2T_x$@CoNi microspheres for tunable electromagnetic wave absorbers

Huanhuan Niu[a], Xuewen Jiang[a], Yongde Xia[b], Hailong Wang[a], Rui Zhang[a,c], Hongxia Li[d], Bingbing Fan[a,*], Yanchun Zhou[a,*]

[a]*School of Material Science & Engineering, Zhengzhou University, Zhengzhou 450001, China*
[b]*Department of Engineering, University of Exeter, Exeter EX4 4SB, UK*
[c]*School of Materials Science and Engineering, Luoyang Institute of Science and Technology, Luoyang 471023, China*
[d]*Sinosteel Luoyang Institute of Refractories Research Co., Ltd., Luoyang 471039, China*

Received: November 17, 2022; Revised: December 30, 2022; Accepted: January 1, 2023

Abstract: $Ti_3C_2T_x$ MXene shows great potential in the application as microwave absorbers due to its high attenuation ability. However, excessively high permittivity and self-stacking are the main obstacles that constrain its wide range of applications. To tackle these problems, herein, the microspheres of SiO_2@$Ti_3C_2T_x$@CoNi with the *hydrangea*-like core–shell structure were designed and prepared by a combinatorial electrostatic assembly and hydrothermal reaction method. These microspheres are constructed by an outside layer of CoNi nanosheets and intermediate $Ti_3C_2T_x$ MXene nanosheets wrapping on the core of modified SiO_2, engendering both homogenous and heterogeneous interfaces. Such trilayer SiO_2@$Ti_3C_2T_x$@CoNi microspheres are "magnetic microsize supercapacitors" that can not only induce dielectric loss and magnetic loss but also provide multilayer interfaces to enhance the interfacial polarization. The optimized impedance matching and core–shell structure could boost the reflection loss (RL) by electromagnetic synergy. The synthesized SiO_2@$Ti_3C_2T_x$@CoNi microspheres demonstrate outstanding microwave absorption (MA) performance benefited from these advantages. The obtained RL value was −63.95 dB at an ultra-thin thickness of 1.2 mm, corresponding to an effective absorption bandwidth (EAB) of 4.56 GHz. This work demonstrates that the trilayer core–shell structure designing strategy is highly efficient for tuning the MA performance of MXene-based microspheres.

Keywords: SiO_2@$Ti_3C_2T_x$@CoNi; *hydrangea*-like core–shell structure; spherical capacitor; high-performance microwave absorption (MA); interfacial polarization; impedance match

1 Introduction

To prevent electromagnetic waves from endangering life and communication security, microwave absorbers have attracted extensive attention [1–4]. Owing to the high intrinsic conductivity, large specific surface area, high electron mobility, and rich surface functional groups and defects, MXenes (two-dimensional (2D) nanosheets formed by etching out A-group element from MAX phases, where M is a transition metal, A is an A-group element, and X is carbon or nitrogen) have

* Corresponding authors.
E-mail: B. Fan, fanbingbing@zzu.edu.cn;
Y. Zhou, yczhou@alum.imr.ac.cn

triggered considerable research interests in using these 2D materials as high-performance microwave absorption (MA) materials [4–9]. However, the high conductivity and self-stacking of $Ti_3C_2T_x$ MXene nanosheets result in the impedance mismatch and thereby weaken the MA properties [10–12]. In addition, the MA performance of MXene-based materials is further hampered by the high permittivity [13].

It has come to light that the characteristic impedance matching and distinct electromagnetic attenuation mechanism are the key points responsible for high MA performance [14]. It is thus conceivable that keeping the surface area of $Ti_3C_2T_x$ MXene nanosheets while taking appropriate strategies to ameliorate the impedance match will enhance the MA performance and promote their application as promising microwave absorbers. To achieve such a goal, numerous tactics have been exploited to address the impedance mismatch and improve the MA capability. For example, the one-dimensional (1D) Ni chain, 2D graphene, and three-dimensional (3D) hollow microspheres were employed to regulate the electromagnetic parameters [15–20]. It has been found that constructing 2D $Ti_3C_2T_x$ MXene nanosheets into 3D core–shell structure can not only hinder self-stacking and supply larger specific surface area but also offer multi-polarization loss mechanism and higher porosity, which provides more scattering and reflection sites and results in the enhanced MA [21–23]. Despite the multiple polarization and proper impedance match provided by the core–shell structure, the monotonous dielectric loss mechanism of $Ti_3C_2T_x$ MXene nanosheets still results in narrow-band MA. To conquer this challenge, magnetic materials have been intercalated, which can achieve effective wide-band MA and enhance microwave attenuation via the synergistic effect of dielectric dissipation and magnetic loss [24–27]. However, the magnetic materials are prone to agglomerating during the synthesis process, leading to a local impedance mismatch. To optimize the benefits of combining the dielectric and magnetic components, it is necessary to design a simple method of $Ti_3C_2T_x$ MXene-based novel magnetic materials.

Supercapacitor is a promising device for energy storage in a wide range of applications. For the MA materials, the supercapacitor structure is beneficial to enhancing the storage capacity, which is conducive to its excellent microwave absorbing properties. Herein, we proposed a strategy to construct the SiO_2, $Ti_3C_2T_x$ MXene nanosheet, and magnetic CoNi alloy into a trilayer core–shell spherical structure, which resembles a micro-size spherical supercapacitor. In this trilayer spherical structure, SiO_2 is crucial in controlling the dielectric constant of $Ti_3C_2T_x$ MXene nanosheet and preventing its self-aggregation, which ensures the impedance matching. Besides, SiO_2 microspheres can also act as a template for core–shell nanosphere formation. To experimentally build the trilayer *hydrangea*-like core–shell structure, a novel electrostatic assembly and hydrothermal method was used in this work. Using this combinatorial method, the agglomeration of the magnetic components is significantly reduced by the strong link formed by electrostatic adsorption between the MXene and CoNi. As we will show in Section 3, the synthesized trilayer SiO_2@$Ti_3C_2T_x$@CoNi microspheres can simultaneously enhance the interfacial polarization and impedance match due to the constructed magnetic coupling network and conductive network, resulting in excellent MA performance. In addition, the microwave reflection and scattering are also enhanced by the unique *hydrangea*-like core–shell structure. The minimum reflection loss (RL) value of the trilayer SiO_2@$Ti_3C_2T_x$@CoNi microspheres is −63.95 dB at an ultra-thin thickness of 1.2 mm, corresponding to an effective absorption bandwidth (EAB) of 4.56 GHz. These results prove the feasibility of designing and synthesizing MXene-based *hydrangea*-like core–shell structured microspheres, which pave the way for producing excellent MA materials.

2 Experimental

2.1 Raw materials

The starting materials were Ti_3AlC_2 particles with 400 mesh in size (Jilin 11 Technology Co., Ltd., China), lithium fluoride (LiF; 99%, Shanghai MacLean Biochemical Co., Ltd., China), ethanol (99.7%) and hydrochloric acid (HCl; 36%–38%) (Luoyang Chemical Tiancheng Reagent Co., Ltd., China), ammonia with analytical purity (Guangdong Xilong Technology Co., Ltd., China), aminopropyl triethoxy silane (3-APTS; Aladdin, China), hydrazine hydrate ($N_2H_4·H_2O$), cobalt chloride ($CoCl_2·6H_2O$), nickel chloride ($NiCl_2·6H_2O$), and methanol (Sinopharm Chemical Reagent Co., Ltd., China). All of the reagents were used without further treatment. The SiO_2 and modified SiO_2 microspheres were prepared by the method reported in Ref. [28].

Briefly, under N_2 environment, 3-APTS was added to the dispersed SiO_2 (prepared by the sol–gel method) ethanol solution and reacted for 10 h at 70 ℃.

2.2 Preparation of *hydrangea*-like core–shell structured SiO_2@$Ti_3C_2T_x$@CoNi microspheres

As the first step, core–shell structured SiO_2@$Ti_3C_2T_x$ was prepared using the method described in Ref. [29]. Briefly, the modified SiO_2 (4 mmol) and $Ti_3C_2T_x$ MXene (10 mL, 5 mg/mL) were mixed and stirred for 1 h to obtain SiO_2@$Ti_3C_2T_x$. Secondly, the SiO_2@$Ti_3C_2T_x$ particles were dispersed in 60 mL of deionized water and agitated for 30 min. After that, 4 mL of $N_2H_4{\cdot}H_2O$ and 5 mL $NH_3{\cdot}H_2O$ were dropwise added while stirring for 30 min, followed by the addition of $NiCl_2{\cdot}6H_2O$ and $CoCl_2{\cdot}6H_2O$ to create homogenous solution. The solution was transferred into a stainless steel autoclave with a Teflon liner and kept at 180 ℃ for 10 h for hydrothermal treatment. Finally, after five rounds of washing in ethanol and deionized water and 8 h of drying, the SiO_2@$Ti_3C_2T_x$@CoNi microspheres with a *hydrangea*-like core–shell structure were produced. The samples were labeled with S_1, S_2, and S_3 based on the injected amounts of Co^{2+} and Ni^{2+} ions at 3, 4, and 5 mmol, respectively. The 2D $Ti_3C_2T_x$@CoNi nanosheets were obtained with the same procedure for the preparation of SiO_2@$Ti_3C_2T_x$@CoNi microspheres except that the SiO_2@$Ti_3C_2T_x$ powders were replaced by $Ti_3C_2T_x$ MXene nanosheet solution (the same mass of $Ti_3C_2T_x$ MXene nanosheets).

2.3 Characterization

The phase compositions of the SiO_2@$Ti_3C_2T_x$@CoNi microspheres were identified by the X-ray diffractometer (Empyrean X, PANalytical B.V., the Netherlands) using Cu Kα radiation (λ = 0.154 nm). The morphologies of the samples were observed in a scanning electron microscope (SEM; JSM-7001F, JEOL, Japan), and the detailed microstructures of the samples were examined in a transmission electron microscope (TEM; JEM-2100F, JEOL, Japan). The presence of the electronic holography was also revealed by the TEM. The surface elemental compositions and chemical bonding of the microspheres were analyzed by using an X-ray photoelectron spectrometer (K-alpha, Thermo Fisher Scientific, USA). To characterize the MA properties, the SiO_2@$Ti_3C_2T_x$@CoNi microspheres (60 wt%) were uniformly mixed with paraffin (40 wt%) to prepare a coaxial ring with an outer diameter of 7.00 mm and an sinner diameter of 3.04 mm. The complex permittivity (ε_r) and permeability (μ_r) of the samples were calculated by a coaxial method using a vector network analyzer (MS46322B, Anli Co., Ltd., Japan).

3 Results and discussion

3.1 Phase composition and microstructure

The *hydrangea*-like core–shell structured SiO_2@$Ti_3C_2T_x$@CoNi microspheres were synthesized feasibly, as illustrated in Fig. 1. Concisely, the SiO_2 and $Ti_3C_2T_x$ MXene were mixed and stirred for 1 h to obtain SiO_2@$Ti_3C_2T_x$. Then the Co^{2+} and Ni^{2+} ions were electrostatically assembled on the surface of SiO_2@$Ti_3C_2T_x$, and the magnetized SiO_2@$Ti_3C_2T_x$@CoNi microspheres were obtained through the hydrothermal reaction.

Figure 2(a) compares the X-ray diffraction (XRD) patterns of the 2D $Ti_3C_2T_x$@CoNi nanosheets and *hydrangea*-like core–shell structured SiO_2@$Ti_3C_2T_x$@CoNi microspheres. Three distinct diffraction peaks at 44.4° (111), 51.7° (200), and 76.3° (220) are indexed to the CoNi alloy, which are between the cubic Co (PDF#15-0806) and cubic Ni (PDF#04-0850) [30]. And the peaks at around 8.3°, 34.7°, and 60.1° can match well with the (002), (008), and (110) planes of the $Ti_3C_2T_x$ MXene nanosheets, respectively.

To demonstrate the presence of $Ti_3C_2T_x$ MXene nanosheets and the magnetic CoNi alloy, the magnetic hysteresis loops and XPS analysis were conducted. The magnetic hysteresis loops (Fig. 2(b)) show that the M values of SiO_2@$Ti_3C_2T_x$@CoNi microspheres and 2D $Ti_3C_2T_x$@CoNi nanosheets are 24.77, 40.51, 53.81, and 94.51 emu/g. The corresponding coercivity values are 116.64, 122.25, 99.96, and 119.29 Ω, respectively, demonstrating that the M values increase with the injected amounts of Co^{2+} and Ni^{2+} ions during the preparation, while those of the coercivity values are comparable. To further confirm the compositions and determine the elemental valence states on the surface of the samples, the XPS analysis was carried out. As shown in Fig. 2(c), the presence of Co, Ni, Ti, Si, C, F, and O signals in SiO_2@$Ti_3C_2T_x$@CoNi microspheres is evident. The Co 2p spectra of the SiO_2@$Ti_3C_2T_x$@CoNi microspheres are shown in Fig. 2(d). The deconvolved peaks at the binding energies of 781.2, 796.5, 797.8, and 803.1 eV correspond to the Co Ni $2p_{3/2}$, Co^{3+} $2p_{1/2}$,

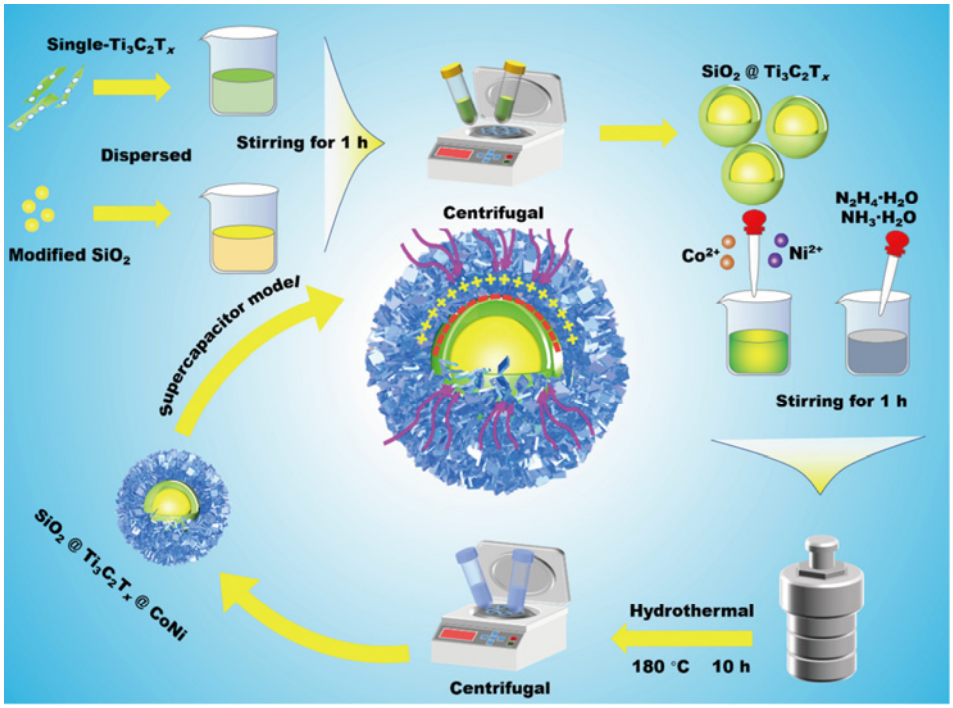

Fig. 1 Illustration of the preparation method for SiO_2@$Ti_3C_2T_x$@CoNi microspheres.

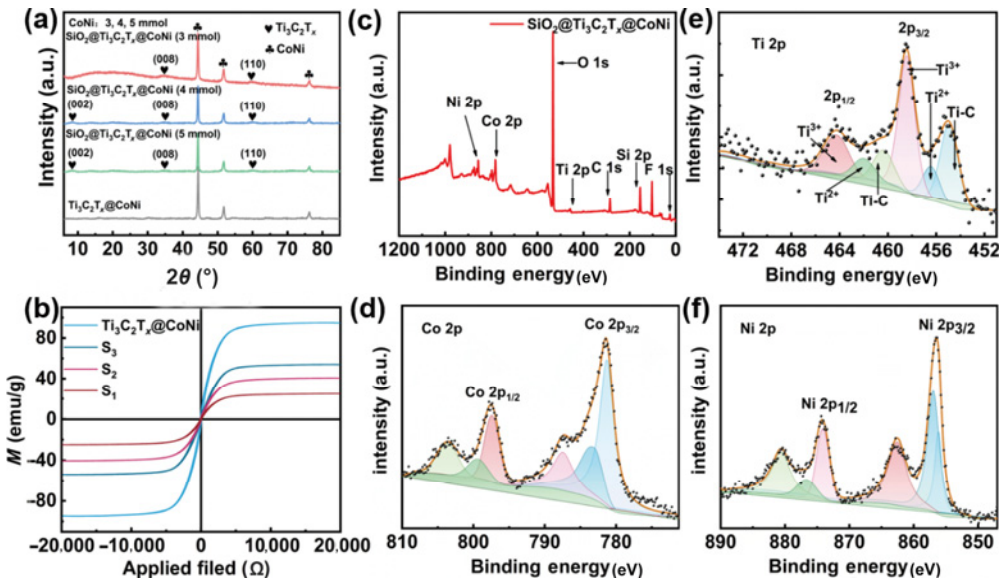

Fig. 2 (a) XRD patterns of 2D $Ti_3C_2T_x$@CoNi nanosheets and SiO_2@$Ti_3C_2T_x$@CoNi microspheres, (b) magnetic hysteresis loops of SiO_2@$Ti_3C_2T_x$@CoNi microspheres and 2D $Ti_3C_2T_x$@CoNi nanosheets (*M* represents the saturation magnetization), (c) X-ray photoelectron spectroscopy (XPS) survey spectra of SiO_2@$Ti_3C_2T_x$@CoNi microspheres (S_2), and (d–f) high-resolution XPS spectra of Co 2p, Ti 2p, and Ni 2p of SiO_2@$Ti_3C_2T_x$@CoNi microspheres (S_2).

Co^{2+} $2p_{1/2}$, and the satellite $2p_{1/2}$ peaks, respectively [31]. Figure 2(e) proves the existence of $Ti_3C_2T_x$. The high-resolution XPS spectra of the Ni element are shown in Fig. 2(f), from which we can attribute the two peaks located at 854.6 and 872.4 eV to Ni $2p_{3/2}$ and Ni $2p_{1/2}$, respectively [32,33]. The above results further prove the existence of CoNi alloy nanosheets in the SiO_2@$Ti_3C_2T_x$@CoNi microspheres. Furthermore, there are no peaks from any impurity phases in the XRD pattern, demonstrating the exceptional purity of the synthesized SiO_2@$Ti_3C_2T_x$@CoNi microspheres.

Based on the foregoing results, the formation of the trilayer structured SiO_2@$Ti_3C_2T_x$@CoNi microspheres through the hydrothermal reactions can be described as

$$Co^{2+} + Ni^{2+} + 4NH_3 \cdot H_2O \rightarrow Co(OH)_2 \downarrow + Ni(OH)_2 \downarrow + 4NH_4^+ \quad (1)$$

$$Co(OH)_2 + Ni(OH)_2 + 8NH_3 \cdot H_2O + 4NH_4^+ \rightarrow [Co(NH_3)_6]^{2+} + [Ni(NH_3)_6]^{2+} + 12H_2O \quad (2)$$

$$[Co(NH_3)_6]_2^{2+} + [Ni_2(NH_3)_6]_2^{2+} + N_2H_4 \rightarrow CoNi + 12NH_3 \uparrow + N_2 \uparrow + 4H^+ \quad (3)$$

During the preparing process, the as-prepared $SiO_2@Ti_3C_2T_x$ nanospheres are rich in functional groups (–OH and –F, as shown in Fig. 3), which makes them easier to provide active sites for the Co^{2+} and Ni^{2+} in an efficient way via the electrostatic force. As a result, a garden of the tiny capacitor was formed between the dielectric SiO_2 core, intermediate $Ti_3C_2T_x$ MXene nanosheets, and metallic layer of CoNi alloy.

The SEM and TEM images of the as-synthesized $SiO_2@Ti_3C_2T_x@CoNi$ microspheres are shown in Fig. 3. The as-synthesized 2D $Ti_3C_2T_x@CoNi$ nanosheets show that CoNi alloy was grown on the surface of $Ti_3C_2T_x$ MXene (Fig. 3(a)). Figure S1 in the Electronic Supplementary Material (ESM) shows the SEM images of multilayer $Ti_3C_2T_x$ MXene (Fig. S1(a)), $Ti_3C_2T_x$ MXene nanosheets (Fig. S1(b)), and SiO_2 microspheres (Fig. S1(c)). In Fig. 3(b), one can see that the core–shell $SiO_2@Ti_3C_2T_x$ microspheres were obtained [29]. During the preparation of $SiO_2@Ti_3C_2T_x@CoNi$ microspheres, the added Co^{2+} and Ni^{2+} ions will be assembled on the surface of the negatively charged $SiO_2@Ti_3C_2T_x$. When $N_2H_4 \cdot H_2O$ was added, the Co^{2+} and Ni^{2+} ions were *in situ* reduced into CoNi nuclei, and $SiO_2@Ti_3C_2T_x@CoNi$ microspheres of *hydrangea*-like core–shell structure (with SiO_2 core, intermediate $Ti_3C_2T_x$ MXene nanosheets, and CoNi alloy shell) were formed (Figs. 3(c)–3(e)). The EDS mappings (Fig. 3(f)) further confirm this result, where the outmost layer is rich in Co and Ni, and the sub-outer layer is rich in Ti, C, F, N, and O. Intriguingly, as shown in Figs. 3(c)–3(e), the size of $SiO_2@Ti_3C_2T_x@CoNi$ microspheres gradually increases with the increasing amount of the added Co^{2+} and Ni^{2+} ions (the addition amounts of Co^{2+} and Ni^{2+} ions were 3, 4, and 5 mmol, forming 110, 250, and 400 nm CoNi alloy shells, respectively), indicating that the T_{CoNi} is tunable through controlling the amount of Co^{2+} and Ni^{2+} ions.

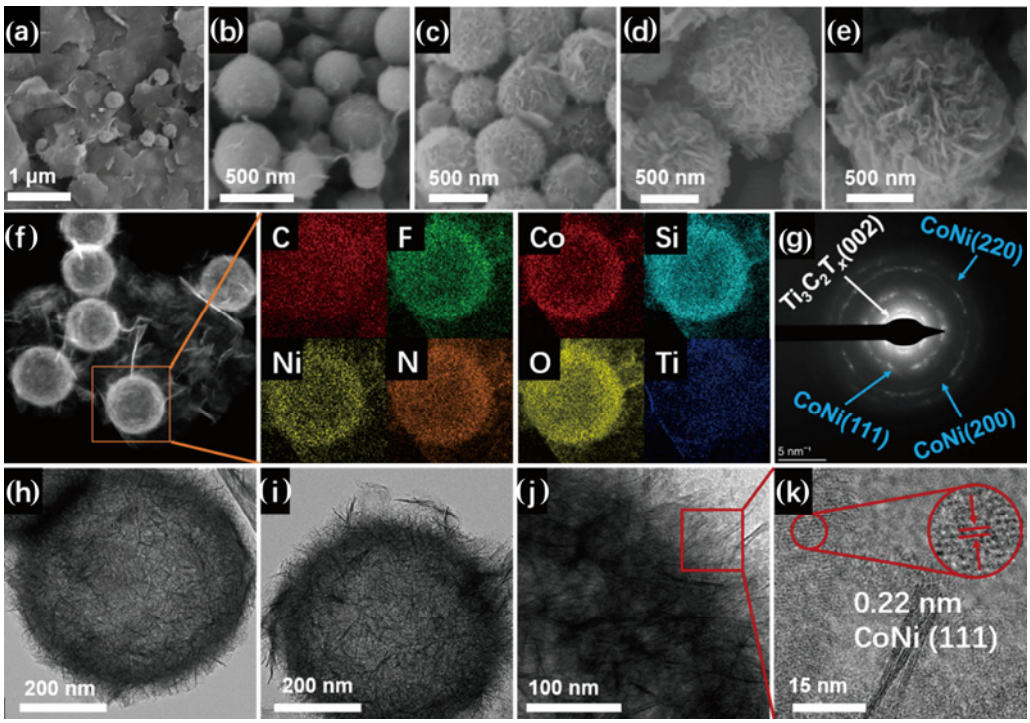

Fig. 3 SEM images of (a) 2D $Ti_3C_2T_x@CoNi$ nanosheets, (b) core–shell structured $SiO_2@Ti_3C_2T_x$ microspheres, and $SiO_2@Ti_3C_2T_x@CoNi$ microspheres with CoNi alloy of different thicknesses T_{CoNi} = (c) 110, (d) 250, and (e) 400 nm. (f) Elemental energy dispersive spectroscopy (EDS) mapping analysis of $SiO_2@Ti_3C_2T_x@CoNi$ microspheres. (g) Selected area electron diffraction (SAED) patterns of $SiO_2@Ti_3C_2T_x@CoNi$ microspheres. (h–j) TEM and (k) high-resolution TEM (HRTEM) images of $SiO_2@Ti_3C_2T_x@CoNi$ microspheres.

The TEM observations were conducted to further examine the detailed microstructures and phase compositions of the SiO_2@$Ti_3C_2T_x$@CoNi microspheres. Figure S2(a) in the ESM shows that the $Ti_3C_2T_x$ MXene nanosheets were obtained after etching and sonicating. In the homologous HRTEM image (Fig. S2(b) in the ESM), the *d*-spacing of 0.241 nm is related to the (103) plane of $Ti_3C_2T_x$ MXene [34]. As shown in Figs. S2(c) and S2(d) in the ESM, rough surfaces of the SiO_2@$Ti_3C_2T_x$ microspheres can be observed, indicating the successful encapsulation of $Ti_3C_2T_x$ MXene nanosheets. Furthermore, the SAED pattern of SiO_2@$Ti_3C_2T_x$@CoNi $Ti_3C_2T_x$ was indexed, which is shown in Fig. 3(g). The four diffraction rings are assigned to the (002) plane of $Ti_3C_2T_x$ and the (111), (200), and (220) planes of CoNi alloy [35]. As shown in Figs. 3(h) and 3(i), the SiO_2@$Ti_3C_2T_x$@CoNi microspheres exhibit a 3D *hydrangea*-like core–shell structure, which may increase the transmission paths of microwaves as well as the interfacial polarization, and maximize the MA properties of the materials. The higher-magnification TEM image of the SiO_2@$Ti_3C_2T_x$@CoNi microspheres (Fig. 3(j)) shows that the CoNi nanosheets are in disarray and uniform conspicuously. As shown in Fig. 3(k), the *d*-spacing of 0.22 nm is corresponding to the (111) plane of CoNi alloy [36]. These results indicate that the SiO_2@$Ti_3C_2T_x$@CoNi microspheres are successfully prepared, and the problem of uneven distribution of CoNi alloy is solved.

3.2 Electromagnetic parameters and MA properties

To evaluate the MA properties, the electromagnetic parameters of 2D $Ti_3C_2T_x$@CoNi nanosheets and SiO_2@$Ti_3C_2T_x$@CoNi microspheres with various contents of CoNi were analyzed. Generally, the ε_r (= $\varepsilon' - j\varepsilon''$) and μ_r (= $\mu' - j\mu''$) determine the MA properties. Among them, the real permittivity (ε') and permeability (μ') represent the capacity of the stored electrical and magnetic energy, and the imaginary permittivity (ε'') and permeability (μ'') reflect the loss ability of energy [37,38]. In the frequency range of 2–18 GHz, the ε' values vary from 15.53 to 19.20 for the 2D $Ti_3C_2T_x$@CoNi nanosheets, and from 15.57 to 19.18, 13.16 to 14.01, and 9.10 to 11.08 for SiO_2@$Ti_3C_2T_x$@CoNi microspheres with CoNi alloy of different thicknesses (Figs. 4(a)–4(d)), while the ε'' values are in the range from 1.87 to 10.10, 3.62 to 9.74, 2.48 to 3.33, and 0.88 to 5.78, respectively. The self-stacking of $Ti_3C_2T_x$ MXene nanosheets has been found to give the 2D $Ti_3C_2T_x$@CoNi nanosheets greater ε_r [39,40]. We have known that the overly large gap between the values of ε' and ε'' of the dielectric constant usually causes impedance mismatching and prevents electromagnetic waves from entering the inside of the

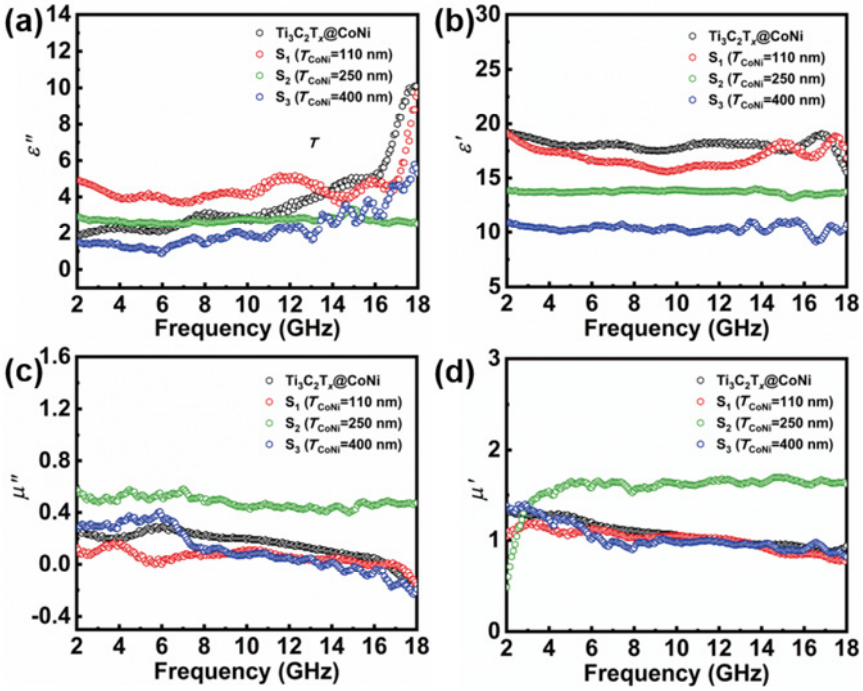

Fig. 4 Connection between electromagnetic parameters ((a) ε'', (b) ε', (c) μ'', and (d) μ') and frequency (f) of 2D $Ti_3C_2T_x$@CoNi nanosheets and SiO_2@$Ti_3C_2T_x$@CoNi microspheres (T_{CoNi} = 110, 250, and 400 nm).

material, which lowers its MA capacity [41]. As can be seen in Fig. 4, due to the establishment of core–shell structure, the gap between the values of ε' and ε'' of SiO_2@$Ti_3C_2T_x$@CoNi microspheres decreased obviously, which is beneficial to improving the impedance matching. As a result, the MA performance of SiO_2@$Ti_3C_2T_x$@CoNi microspheres is superior to that of 2D $Ti_3C_2T_x$@CoNi nanosheets. Furthermore, both the ε' and ε'' for SiO_2@$Ti_3C_2T_x$@CoNi microspheres show several fluctuations over the whole frequency range, which are attributed to the dielectric polarization relaxation behavior [42,43]. Figures 4(c) and 4(d) show that the μ' and μ'' values of SiO_2@$Ti_3C_2T_x$@CoNi microspheres (T_{CoNi} = 250 nm) are the largest among these samples, indicating excellent magnetic loss. In addition, the phase hysteresis between capacitance and inductance on the core–shell structure might be responsible for the negative μ'' at high frequencies [44].

Undoubtedly, the dielectric–magnetic coupled loss plays a key role in terms of improving the MA capacity. Figure 5(a) reveals that the dielectric loss tangents ($\tan\delta_\varepsilon = \varepsilon'/\varepsilon''$) of SiO_2@$Ti_3C_2T_x$@CoNi (T_{CoNi} = 110 nm) and SiO_2@$Ti_3C_2T_x$@CoNi (T_{CoNi} = 250 nm) are higher than SiO_2@$Ti_3C_2T_x$@CoNi (T_{CoNi} = 400 nm) and 2D $Ti_3C_2T_x$@CoNi nanosheets in most frequency bands, demonstrating that the overdosage of CoNi alloy would weaken the dielectric loss ability. Owing to the well-distributed CoNi alloy on the surface of the microspheres, themagnetic loss (C_0) and magnetic loss tangent ($\tan\delta_\mu = \mu''/\mu'$) of SiO_2@$Ti_3C_2T_x$@CoNi microspheres (T_{CoNi} = 250 nm) is much higher than that of 2D $Ti_3C_2T_x$@CoNi nanosheets (Fig. 5(b)), thereby leading to the enhanced MA performance. Moreover, the rich interfaces in trilayer SiO_2@$Ti_3C_2T_x$@CoNi microspheres are formed by the unique 3D *hydrangea*-like core–shell structure, which considerably enhances the interfacial polarization. The aforementioned results demonstrate that the electromagnetic parameters can be adjusted by constructing the core–shell structure and adding an appropriate amount of evenly distributed alloy, which could improve the impedance matching and enhance the MA performance.

The 3D graphs of RL values against f and thickness are shown in Fig. 6, which are evaluated by Eqs. (4) and (5) [45,46]:

$$\mathrm{RL} = 20\log\left|\frac{Z_{\mathrm{in}} - Z_0}{Z_{\mathrm{in}} + Z_0}\right| \tag{4}$$

$$Z_{\mathrm{in}} = Z_0\sqrt{\frac{\mu_{\mathrm{r}}}{\varepsilon_{\mathrm{r}}}}\tanh\left(\mathrm{j}\left(\frac{2\pi fd}{c}\right)\sqrt{\mu_{\mathrm{r}}\varepsilon_{\mathrm{r}}}\right) \tag{5}$$

where Z_{in}, d, and Z_0 represent the input impedance, the thickness of a material, and the air impedance, respectively. Generally, an excellent MA material should demonstrate a broad EAB with an ultra-thin thickness.

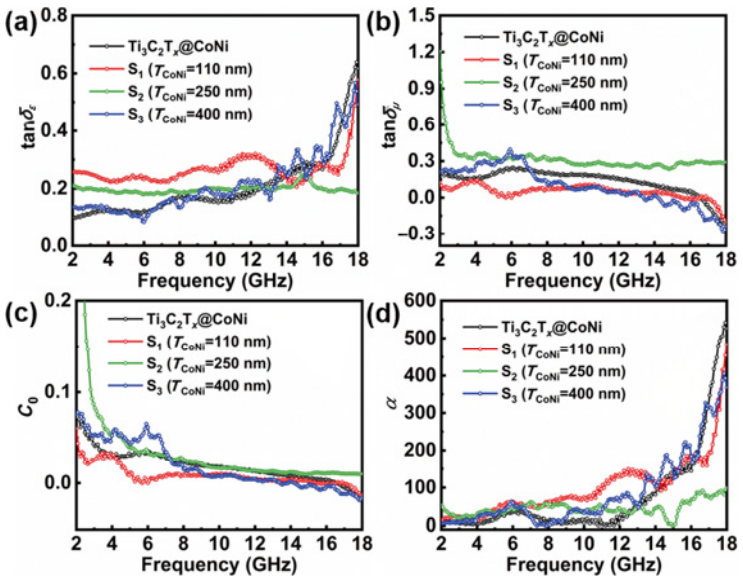

Fig. 5 (a) $\tan\delta_\varepsilon$, (b) $\tan\delta_\mu$, (c) correlation of frequency ($C_0 = \mu''\mu'^{-2}f^{-1}$), and (d) frequency dependence of attenuation constant ($\alpha = \frac{\sqrt{2}\pi f}{c}\sqrt{\mu''\varepsilon'' - \mu'\varepsilon' + \sqrt{(\mu''\varepsilon'' - \mu'\varepsilon')^2 + (\mu'\varepsilon'' + \mu''\varepsilon')^2}}$, where c represents the speed of light) of 2D $Ti_3C_2T_x$@CoNi nanosheets and samples of SiO_2@$Ti_3C_2T_x$@CoNi microspheres.

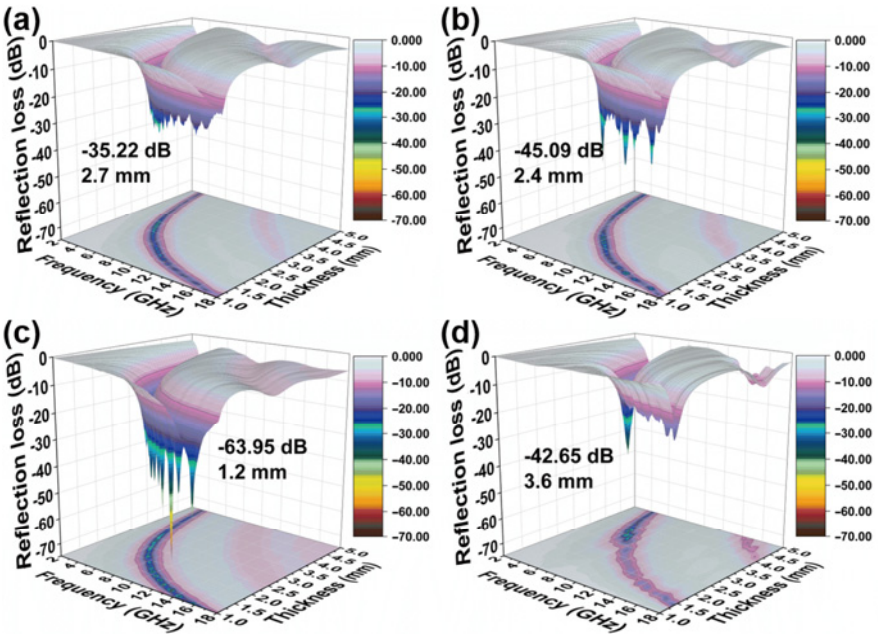

Fig. 6 3D RL curves and contour mappings of (a) 2D $Ti_3C_2T_x$@CoNi nanosheets and (b–d) SiO_2@$Ti_3C_2T_x$@CoNi microspheres with CoNi alloy of different thicknesses (T_{CoNi} = 110, 250, and 400 nm).

Due to the 3D *hydrangea*-like core–shell structure and uniformly dispersed CoNi alloy, the optimal RL value of SiO_2@$Ti_3C_2T_x$@CoNi microspheres has been significantly improved. Notably, the strongest RL value of SiO_2@$Ti_3C_2T_x$@CoNi microspheres (T_{CoNi} = 250 nm) achieves −63.95 dB at an ultra-thin thickness of 1.2 mm, corresponding to an EAB of 4.56 GHz (Fig. 7(a)). The EAB fluctuates around 15.13 GHz in the thickness range of 1–5 mm (Fig. S3 in the ESM). Conversely, the 2D $Ti_3C_2T_x$@CoNi nanosheets only reach a limited RL value of −35.22 dB at 2.7 mm. It is obvious that the SiO_2@$Ti_3C_2T_x$@CoNi microspheres (T_{CoNi} = 250 nm) exhibit much better MA properties than other reported MXene-based magnetic materials (Fig. 7(c)) [37,41,47–58].

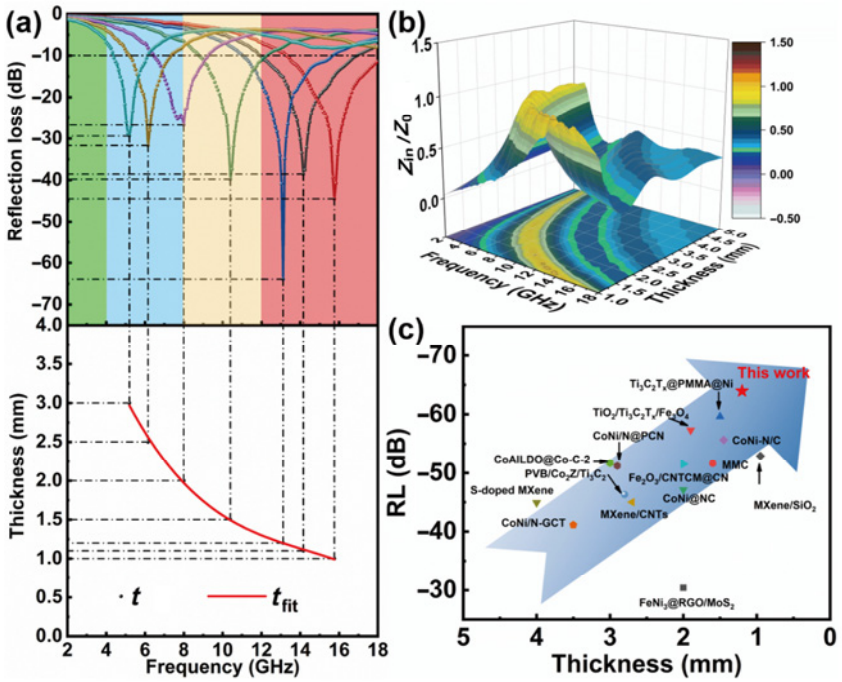

Fig. 7 (a) MA properties and corresponding thickness simulation and (b) Z_{in}/Z_0 of SiO_2@$Ti_3C_2T_x$@CoNi (T_{CoNi} = 250 nm). (c) RL comparison with reported MXene-based or magnetic materials.

3. 3 Mechanisms for enhanced MA properties

The appropriate attenuation loss is a prerequisite for an excellent MA material. According to Refs. [59–62], the superior MA materials generally possess appropriate complex dielectric constants ($\varepsilon' = 5–20$ and $\varepsilon'' = 1–10$) and an optimal α ($\approx 25–350$). In Fig. 5(d), it is evident that the α values of SiO_2@$Ti_3C_2T_x$@CoNi (T_{CoNi} = 250 nm) fulfill this condition well, while the values of 2D $Ti_3C_2T_x$@CoNi nanosheets are over 350 in the high frequency range. Thus, we can conclude at this point that the α values are tunable by controlling the morphology of the micro-particles and the distribution uniformity of CoNi alloy, which enhances the MA properties of MXene-based materials.

The other precondition for subsequently dissipating the incident waves is the favorable impedance match [63]. High MA performance can be realized when the impedance of the absorber (Z_{in}) is equal to the impedance of free space (Z_0) [64]. The values of impedance match ($Z = Z_{in}/Z_0$) between 0.8 and 1.2 can be found over all f of the impedance match diagrams of $SiO_2Ti_3C_2T_x$@CoNi (T_{CoNi} = 250 nm) (Fig. 7(b)), which is an indicator of excellent MA properties [65]. However, the impedance match values of 2D $Ti_3C_2T_x$@CoNi nanosheets and SiO_2@$Ti_3C_2T_x$@CoNi microspheres (T_{CoNi} = 110 nm) are below 0.8, and the values of SiO_2@$Ti_3C_2T_x$@CoNi microspheres (T_{CoNi} = 400 nm) are above 1.2 in most frequency ranges (Fig. S4 in the ESM), resulting in big impedance mismatch. Therefore, uniform distribution of suitable amounts of CoNi alloy can improve the impedance matching. In addition, the construction of core–shell structure breaks the conductive network and further reduces the permittivity, leading to remarkable melioration of impedance matching. Due to the above advantages, the MA performance of SiO_2@$Ti_3C_2T_x$@CoNi (T_{CoNi} = 250 nm) is significantly improved.

The excellent MA properties of an absorber are also determined by polarization loss. The intrinsic dipoles originated from the functional groups of –OH and –F, and the numerous defects on the surface of $Ti_3C_2T_x$ MXene nanosheets can serve as polarization centers combiningand generate dipolar polarization and defect-induced polarization, thereby absorbing the incident microwave radiation [66]. Besides, the combining and coupling of different materials are easy to create heterogeneous ($Ti_3C_2T_x$/SiO_2 and $Ti_3C_2T_x$/CoNi interfaces) or homogeneous interfaces (CoNi/CoNi and $Ti_3C_2T_x$/$Ti_3C_2T_x$ interfaces), as shown in Fig. 8, which induct interfacial polarization. Based on the function of suppressed cumulation and the accessible interface of $Ti_3C_2T_x$ MXene, the unique *hydrangea*-like core–shell structure of SiO_2@$Ti_3C_2T_x$@CoNi microspheres is favorable for strengthening the interfacial polarization. Thus, SiO_2@$Ti_3C_2T_x$@CoNi microspheres can be regarded as a spherical super micro-capacitor composed of SiO_2, MXene, and CoNi alloy, which will also boost the interfacial polarization effect.

To further probe the interfacial polarization of the *hydrangea*-like core–shell heterostructure deeply, the off-axis holography (Fig. 8) is exploited to characterize the distribution of charge density at the spatial potential [67]. The technique of off-axis electron hologram can form an interference pattern, which is generated by overlapping part of the electron wave that has passed

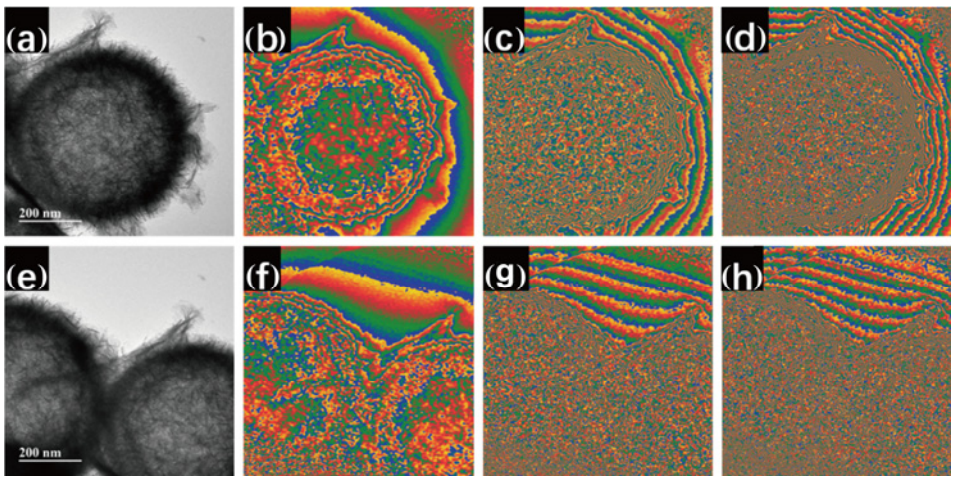

Fig. 8 (a, e) TEM images and corresponding off-axis electron holograms of (b–d) spatial potential and (f–h) charge density of SiO_2@$Ti_3C_2T_x$@CoNi microspheres.

unperturbed through vacuum (reference waves) with another part of the electron wave that has passed through the sample (object waves). The resulting interference patterns encode the phase shift between the object and reference waves, which can be utilized to reveal local differences in electrostatic potential within and around the specimen [68]. Figure 8 shows the TEM images and the corresponding charge density images under various amplified external electromagnetic fields. It is evident that the charges accumulate around (Figs. 8(b)–8(d)) and between (Figs. 8(f)–8(h)) the tiny capacitors with the continuous amplification of the signal, leading to strong interfacial polarization [49,69]. Moreover, under the action of external electromagnetic fields, multiple carriers can migrate and accumulate rapidly around the heterogeneous and homogeneous interfaces, which leads to the unbalance of charge distribution and the establishment of internal electric fields between MXene and CoNi alloys in each 3D microsphere unit, thus promoting the strong interfacial polarization loss [70]. Compared with those among the single component, the interfaces formed among the *hydrangea*-like core–shell structure are more abundant and provide intensive and reinforced interfacial polarization, thereby dissipating the incident microwave energy. Therefore, such multiple polarizations drive the enhancement of MA performance.

The excellent absorbing performance of SiO_2@$Ti_3C_2T_x$@CoNi microspheres is inseparable from the loss mechanism brought by the material design, which is outlined in Fig. 9. As shown in Fig. 9,

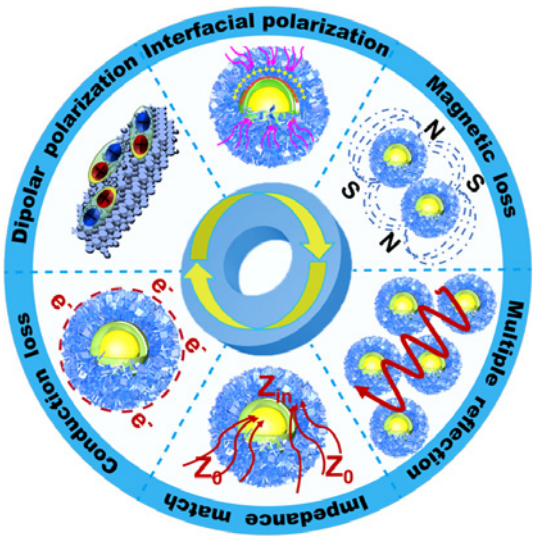

Fig. 9 Proposed electromagnetic wave absorption mechanisms of SiO_2@$Ti_3C_2T_x$@CoNi microspheres.

the unique structure promotes the absorption of microwaves overshielding and attenuates microwave radiation through conduction loss and polarization loss. Moreover, the even distribution of magnetic units in the synthesized SiO_2@$Ti_3C_2T_x$@CoNi can effectively improve the spatial magnetic distribution, thereby further enhancing the magnetic loss mechanism in the composite materials. Hence, superior MA performance is achieved by introducing multiple loss mechanisms caused by core–shell structure and electromagnetic synergistic effect.

4 Conclusions

Using a combinatorial electrostatic assembly and hydrothermal reaction method, trilayer *hydrangea*-like MXene-based core–shell SiO_2@$Ti_3C_2T_x$@CoNi microspheres are prepared, in which the $Ti_3C_2T_x$ MXene nanosheets are dispersed on top of the modified SiO_2 spheres, and numerous magnetic CoNi nanoflakes are uniformly grown on the surface of $Ti_3C_2T_x$. The obtained SiO_2@$Ti_3C_2T_x$@CoNi microspheres demonstrate exceptionally good MA performance with an RL value of −63.95 dB at an ultra-thin thickness (~1.2 mm), corresponding to an EAB of 4.56 GHz. Such a novel structure concurrently enhances the interfacial polarization by forming the trilayer SiO_2@$Ti_3C_2T_x$@CoNi interfaces, optimizes the impedance matching by modified SiO_2 and core–shell structure, and boosts the RL by electromagnetic synergy. These results highlight that the outstanding MA performance is doubtlessly attributed to the noteworthy preponderances of structural features of the SiO_2@$Ti_3C_2T_x$@CoNi microspheres. In conclusion, this work provides an innovative hierarchical structure design strategy for MXene-based composites with high-efficient MA performance.

Acknowledgements

This work was supported by the National Natural Science Foundation of China (U2004177), the Outstanding Youth Fund of Henan Province (212300410081), and the Science and Technology Innovation Talents in Universities of Henan Province (CN) (22HASTIT001). Bingbing Fan also acknowledged the financial support from the Research and Entrepreneurship Start-up Projects for Overseas Returned Talents.

Declaration of competing interest

The authors have no competing interests to declare that are relevant to the content of this article.

Electronic Supplementary Material

Supplementary material is available in the online version of this article at https://doi.org/10.26599/JAC.2023.9220714.

References

[1] Wang GH, Ong SJH, Zhao Y, *et al*. Integrated multifunctional macrostructures for electromagnetic wave absorption and shielding. *J Mater Chem A* 2020, **8**: 24368–24387.

[2] Chen XT, Zhou M, Zhao Y, *et al*. Morphology control of eco-friendly chitosan-derived carbon aerogels for efficient microwave absorption at thin thickness and thermal stealth. *Green Chem* 2022, **24**: 5280–5290.

[3] Zhang M, Ling HL, Wang T, *et al*. An equivalent substitute strategy for constructing 3D ordered porous carbon foams and their electromagnetic attenuation mechanism. *Nano-Micro Lett* 2022, **14**: 157.

[4] Fang YS, Yuan J, Liu TT, *et al*. Clipping electron transport and polarization relaxation of $Ti_3C_2T_x$ based nanocomposites towards multifunction. *Carbon* 2023, **201**: 371–380.

[5] Song Q, Ye F, Kong L, *et al*. Graphene and MXene nanomaterials: Toward high-performance electromagnetic wave absorption in gigahertz band range. *Adv Funct Mater* 2020, **30**: 2000475.

[6] Cao MS, Cai YZ, He P, *et al*. 2D MXenes: Electromagnetic property for microwave absorption and electromagnetic interference shielding. *Chem Eng J* 2019, **359**: 1265–1302.

[7] Lu YH, Zhang SL, He MY, *et al*. 3D cross-linked graphene or/and MXene based nanomaterials for electromagnetic wave absorbing and shielding. *Carbon* 2021, **178**: 413–435.

[8] Zhang ZW, Cai ZH, Zhang Y, *et al*. The recent progress of MXene-based microwave absorption materials. *Carbon* 2021, **174**: 484–499.

[9] Du H, Zhang QP, Zhao B, *et al*. Novel hierarchical structure of $MoS_2/TiO_2/Ti_3C_2T_x$ composites for dramatically enhanced electromagnetic absorbing properties. *J Adv Ceram* 2021, **10**: 1042–1051.

[10] Wu ZC, Tian K, Huang T, *et al*. Hierarchically porous carbons derived from biomasses with excellent microwave absorption performance. *ACS Appl Mater Interfaces* 2018, **10**: 11108–11115.

[11] Wang XH, Chen YQ, Hu FY, *et al*. Electromagnetic interference shielding performance of flexible, hydrophobic honeycomb-structured $Ag@Ti_3C_2T_x$ composites. *Adv Electron Mater* 2022, **8**: 2101028.

[12] Wu XY, Tu TX, Dai Y, *et al*. Direct ink writing of highly conductive MXene frames for tunable electromagnetic interference shielding and electromagnetic wave-induced thermochromism. *Nano-Micro Lett* 2021, **13**: 148.

[13] Wang XH, Bao S, Hu FY, *et al*. The effect of honeycomb pore size on the electromagnetic interference shielding performance of multifunctional 3D honeycomb-like $Ag/Ti_3C_2T_x$ hybrid structures. *Ceram Int* 2022, **48**: 16892–16900.

[14] Wang SJ, Li DS, Zhou Y, *et al*. Hierarchical $Ti_3C_2T_x$ MXene/Ni chain/ZnO array hybrid nanostructures on cotton fabric for durable self-cleaning and enhanced microwave absorption. *ACS Nano* 2020, **14**: 8634–8645.

[15] Deng BW, Liu ZC, Pan F, *et al*. Electrostatically self-assembled two-dimensional magnetized MXene/hollow Fe_3O_4 nanoparticle hybrids with high electromagnetic absorption performance and improved impendence matching. *J Mater Chem A* 2021, **9**: 3500–3510.

[16] Wang HY, Sun XB, Yang SH, *et al*. 3D ultralight hollow NiCo compound@MXene composites for tunable and high-efficient microwave absorption. *Nano-Micro Lett* 2021, **13**: 206.

[17] Xiang Z, Shi YY, Zhu XJ, *et al*. Flexible and waterproof 2D/1D/0D construction of MXene-based nanocomposites for electromagnetic wave absorption, EMI shielding, and photothermal conversion. *Nano-Micro Lett* 2021, **13**: 150.

[18] Tao JQ, Xu LL, Jin HS, *et al*. Selective coding dielectric genes based on proton tailoring to improve microwave absorption of MOFs. *Adv Powder Mater* 2023, **2**: 100091.

[19] Guan XM, Yang ZH, Zhou M, *et al*. 2D MXene nanomaterials: Synthesis, mechanism, and multifunctional applications in microwave absorption. *Small Struct* 2022, **3**: 2200102.

[20] Wang QQ, Niu B, Han YH, *et al*. Nature-inspired 3D hierarchical structured "vine" for efficient microwave attenuation and electromagnetic energy conversion device. *Chem Eng J* 2023, **452**: 139042.

[21] Wang FY, Wang N, Han XJ, *et al*. Core–shell FeCo@carbon nanoparticles encapsulated in polydopamine-derived carbon nanocages for efficient microwave absorption. *Carbon* 2019, **145**: 701–711.

[22] Guo Y, Jian X, Zhang L, *et al*. Plasma-induced $FeSiAl@Al_2O_3@SiO_2$ core–shell structure for exceptional microwave absorption and anti-oxidation at high temperature. *Chem Eng J* 2020, **384**: 123371.

[23] Liu QH, Cao Q, Bi H, *et al*. $CoNi@SiO_2@TiO_2$ and CoNi@air@TiO_2 microspheres with strong wideband microwave absorption. *Adv Mater* 2016, **28**: 486–490.

[24] Liu Y, Jia ZR, Zhan QQ, *et al*. Magnetic manganese-based composites with multiple loss mechanisms towards broadband absorption. *Nano Res* 2022, **15**: 5590–5600.

[25] Yuan M, Zhou M, Fu HQ. Synergistic microstructure of sandwich-like $NiFe_2O_4@SiO_2@$MXene nanocomposites for enhancement of microwave absorption in the whole Ku-band. *Compos Part B-Eng* 2021, **224**: 109178.

[26] Li ZJ, Lin H, Xie YX, *et al*. Monodispersed Co@C

nanoparticles anchored on reclaimed carbon black toward high-performance electromagnetic wave absorption. *J Mater Sci Technol* 2022, **124**: 182–192.

[27] Ma ML, Liao ZJ, Su XW, *et al*. Magnetic CoNi alloy particles embedded N-doped carbon fibers with polypyrrole for excellent electromagnetic wave absorption. *J Colloid Interf Sci* 2022, **608**: 2203–2212.

[28] Liu JW, Zhang Q, Chen XW, *et al*. Surface assembly of graphene oxide nanosheets on SiO_2 particles for the selective isolation of hemoglobin. *Chemistry* 2011, **17**: 4864–4870.

[29] Niu HH, Tu XY, Zhang S, *et al*. Engineered core–shell SiO_2@$Ti_3C_2T_x$ composites: Towards ultra-thin electromagnetic wave absorption materials. *Chem Eng J* 2022, **446**: 137260.

[30] Liang XH, Man ZM, Quan B, *et al*. Environment-stable Co_xNi_y encapsulation in stacked porous carbon nanosheets for enhanced microwave absorption. *Nano-Micro Lett* 2020, **12**: 102.

[31] Zhang X, Yan F, Zhang S, *et al*. Hollow N-doped carbon polyhedron containing CoNi alloy nanoparticles embedded within few-layer N-doped graphene as high-performance electromagnetic wave absorbing material. *ACS Appl Mater Interfaces* 2018, **10**: 24920–24929.

[32] He N, He ZD, Liu L, *et al*. Ni^{2+} guided phase/structure evolution and ultra-wide bandwidth microwave absorption of Co_xNi_{1-x} alloy hollow microspheres. *Chem Eng J* 2020, **381**: 122743.

[33] Zhang N, Huang Y, Wang MY, *et al*. Design and microwave absorption properties of thistle-like CoNi enveloped in dielectric Ag decorated graphene composites. *J Colloid Interf Sci* 2019, **534**: 110–121.

[34] Li X, Wen CY, Yang LT, *et al*. MXene/FeCo films with distinct and tunable electromagnetic wave absorption by morphology control and magnetic anisotropy. *Carbon* 2021, **175**: 509–518.

[35] Sun GB, Wu H, Liao QL, *et al*. Enhanced microwave absorption performance of highly dispersed CoNi nanostructures arrayed on graphene. *Nano Res* 2018, **11**: 2689–2704.

[36] Wu YH, Peng KS, Man ZM, *et al*. A hierarchically three-dimensional CoNi/N-doped porous carbon nanosheets with high performance of electromagnetic wave absorption. *Carbon* 2022, **188**: 503–512.

[37] Yu XF, Zhang Y, Wang L, *et al*. Improved microwave absorption performance of a multi-dimensional Fe_2O_3/CNTCM@CN assembly achieved by enhanced dielectric relaxation. *J Mater Chem C* 2020, **8**: 5715–5726.

[38] Wang L, Li X, Li QQ, *et al*. Enhanced polarization from hollow cube-like $ZnSnO_3$ wrapped by multiwalled carbon nanotubes: As a lightweight and high-performance microwave absorber. *ACS Appl Mater Interfaces* 2018, **10**: 22602–22610.

[39] He P, Cao MS, Cai YZ, *et al*. Self-assembling flexible 2D carbide MXene film with tunable integrated electron migration and group relaxation toward energy storage and green EMI shielding. *Carbon* 2020, **157**: 80–89.

[40] Yun T, Kim H, Iqbal A, *et al*. Electromagnetic shielding of monolayer MXene assemblies. *Adv Mater* 2020, **32**: 1906769.

[41] Guo R, Fan YC, Wang LJ, *et al*. Core–rim structured carbide MXene/SiO_2 nanoplates as an ultrathin microwave absorber. *Carbon* 2020, **169**: 214–224.

[42] Man ZM, Li P, Zhou D, *et al*. Two birds with one stone: FeS_2@C yolk–shell composite for high-performance sodium-ion energy storage and electromagnetic wave absorption. *Nano Lett* 2020, **20**: 3769–3777.

[43] Wang JW, Jia ZR, Liu XH, *et al*. Construction of 1D heterostructure NiCo@C/ZnO nanorod with enhanced microwave absorption. *Nano-Micro Lett* 2021, **13**: 175.

[44] Zhang S, Zhang F, Xie YY, *et al*. Ultrathin CoNi@$Ti_3C_2T_x$ composites with sandwich structures for efficient microwave absorption. *Ceram Int* 2022, **48**: 33751–33762.

[45] Hu FY, Zhang F, Wang XH, *et al*. Ultrabroad band microwave absorption from hierarchical MoO_3/TiO_2/$Mo_2TiC_2T_x$ hybrids via annealing treatment. *J Adv Ceram* 2022, **11**: 1466–1478.

[46] Ma ML, Bi YX, Jiao ZG, *et al*. Facile fabrication of metal–organic framework derived Fe/Fe_3O_4/FeN/N-doped carbon composites coated with PPy for superior microwave absorption. *J Colloid Interf Sci* 2022, **608**: 525–535.

[47] Ding X, Huang Y, Li SP, *et al*. $FeNi_3$ nanoalloy decorated on 3D architecture composite of reduced graphene oxide/molybdenum disulfide giving excellent electromagnetic wave absorption properties. *J Alloys Compd* 2016, **689**: 208–217.

[48] Wu F, Liu ZH, Wang JQ, *et al*. Template-free self-assembly of MXene and CoNi-bimetal MOF into intertwined one-dimensional heterostructure and its microwave absorbing properties. *Chem Eng J* 2021, **422**: 130591.

[49] Wen CY, Li X, Zhang RX, *et al*. High-density anisotropy magnetism enhanced microwave absorption performance in $Ti_3C_2T_x$ MXene@Ni microspheres. *ACS Nano* 2022, **16**: 1150–1159.

[50] Shen ZJ, Yang HL, Xiong ZQ, *et al*. Hollow core–shell CoNi@C and CoNi@NC composites as high-performance microwave absorbers. *J Alloys Compd* 2021, **871**: 159574.

[51] Liang LL, Liu Z, Xie LJ, *et al*. Bamboo-like N-doped carbon tubes encapsulated CoNi nanospheres towards efficient and anticorrosive microwave absorbents. *Carbon* 2021, **171**: 142–153.

[52] Cui YH, Wu F, Wang JQ, *et al*. Three dimensional porous MXene/CNTs microspheres: Preparation, characterization and microwave absorbing properties. *Compos Part A-Appl S* 2021, **145**: 106378.

[53] Cui YH, Yang K, Wang JQ, *et al*. Preparation of pleated rGO/MXene/Fe_3O_4 microsphere and its absorption properties for electromagnetic wave. *Carbon* 2021, **172**: 1–14.

[54] Wu JD, Feng Y, Xia Y, *et al*. Fabrication of S-doped $Ti_3C_2T_x$ materials with enhanced electromagnetic wave absorbing properties. *J Alloys Compd* 2022, **891**: 161942.

[55] Zhang XC, Zhang X, Yuan HR, *et al*. CoNi nanoparticles encapsulated by nitrogen-doped carbon nanotube arrays on

reduced graphene oxide sheets for electromagnetic wave absorption. *Chem Eng J* 2020, **383**: 123208.

[56] Yang HB, Dai JJ, Liu X, *et al*. Layered PVB/$Ba_3Co_2Fe_{24}O_{41}$/Ti_3C_2 MXene composite: Enhanced electromagnetic wave absorption properties with high impedance match in a wide frequency range. *Mater Chem Phys* 2017, **200**: 179–186.

[57] Zhang XF, Wang ZY, Xu LL, *et al*. Liquid metal derived MOF functionalized nanoarrays with ultra-wideband electromagnetic absorption. *J Colloid Interf Sci* 2022, **606**: 1852–1865.

[58] Liu PJ, Ng VMH, Yao ZJ, *et al*. Ultrasmall Fe_3O_4 nanoparticles on MXenes with high microwave absorption performance. *Mater Lett* 2018, **229**: 286–289.

[59] Yin XW, Kong L, Zhang LT, *et al*. Electromagnetic properties of Si–C–N based ceramics and composites. *Int Mater Rev* 2014, **59**: 326–355.

[60] Shu RW, Wan ZL, Zhang JB, *et al*. Facile design of three-dimensional nitrogen-doped reduced graphene oxide/multi-walled carbon nanotube composite foams as lightweight and highly efficient microwave absorbers. *ACS Appl Mater Interfaces* 2020, **12**: 4689–4698.

[61] Ge CQ, Wang LY, Liu G, *et al*. Enhanced electromagnetic properties of carbon nanotubes and SiO_2-coated carbonyl iron microwave absorber. *J Alloys Compd* 2018, **767**: 173–180.

[62] Wang Y, Gao X, Zhang LJ, *et al*. Synthesis of Ti_3C_2/Fe_3O_4/PANI hierarchical architecture composite as an efficient wide-band electromagnetic absorber. *Appl Surf Sci* 2019, **480**: 830–838.

[63] Wu Y, Zhao Y, Zhou M, *et al*. Ultrabroad microwave absorption ability and infrared stealth property of nano-micro CuS@rGO lightweight aerogels. *Nano-Micro Lett* 2022, **14**: 171.

[64] Gu WH, Ong SJH, Shen YH, *et al*. A lightweight, elastic, and thermally insulating stealth foam with high infrared-radar compatibility. *Adv Sci* 2022, **9**: 2204165.

[65] Huang YQ, Yuan J, Song WL, *et al*. Microwave absorbing materials: Solutions for real functions under ideal conditions of microwave absorption. *Chin Phys Lett* 2010, **27**: 027702.

[66] Qiu X, Wang LX, Zhu HL, *et al*. Lightweight and efficient microwave absorbing materials based on walnut shell-derived nano-porous carbon. *Nanoscale* 2017, **9**: 7408–7418.

[67] Liu PB, Gao S, Zhang GZ, *et al*. Hollow engineering to Co@N-doped carbon nanocages via synergistic protecting–etching strategy for ultrahigh microwave absorption. *Adv Funct Mater* 2021, **31**: 2102812.

[68] Yazdi S, Kasama T, Beleggia M, *et al*. Towards quantitative electrostatic potential mapping of working semiconductor devices using off-axis electron holography. *Ultramicroscopy* 2015, **152**: 10–20.

[69] Song LM, Zhang F, Chen YQ, *et al*. Multifunctional SiC@SiO_2 nanofiber aerogel with ultrabroadband electromagnetic wave absorption. *Nano-Micro Lett* 2022, **14**: 152.

[70] Li X, You WB, Xu CY, *et al*. 3D seed-germination-like MXene with *in situ* growing CNTs/Ni heterojunction for enhanced microwave absorption via polarization and magnetization. *Nano-Micro Lett* 2021, **13**: 157.